Received: 20 December 2023 | Revised: 20 February 2024 | Accepted: 22 February 2024

DOI: 10.1002/esp.5816

RESEARCH ARTICLE

ESPL WILEY

The effect of location and geometric properties of landslides caused by rainstorms and earthquakes

Haijun Qiu[1,2] | Lingling Su[1] | Bingzhe Tang[1,2] | Dongdong Yang[1,2] | Mohib Ullah[1] | Yaru Zhu[1] | Ulrich Kamp[3]

[1]Shaanxi Key Laboratory of Earth Surface System and Environmental Carrying Capacity, College of Urban and Environmental Sciences, Northwest University, Xi'an, China

[2]Institute of Earth Surface System and Hazards, College of Urban and Environmental Sciences, Northwest University, Xi'an, China

[3]Earth and Environment Discipline, Department of Natural Sciences, University of Michigan-Dearborn, Dearborn, Michigan, USA

Correspondence
Haijun Qiu, Shaanxi Key Laboratory of Earth Surface System and Environmental Carrying Capacity, College of Urban and Environmental Sciences, Northwest University, Xi'an 710127, China.
Email: haijunqiu@nwu.edu.cn

Funding information
National Natural Science Foundation of China, Grant/Award Number: 42271078; Selected Science and Technology Activity Program for Overseas Scientists, Grant/Award Number: 2022-14; Key Research and Development Program of Shaanxi, Grant/Award Number: 2024SF-YBXM-669; The Second Tibetan Plateau Scientific Expedition and Research Program (STEP), Grant/Award Number: 2019QZKK0902

Abstract

Landslides triggered by rainstorms and earthquakes are prominent geological hazards that exhibit distinctive spatial and morphological characteristics due to diverse instability mechanisms. However, studies on differences between the two types of landslides remain limited. In this study, we explored differences in location and geometric properties between rainstorm-induced landslides in Qinzhou, Longchuan and Fukuoka and earthquake-induced landslides in Lushan, Iburi and Kaikōura. We normalized the location of landslides across the slope and quantified the landslide polygons using four geometric properties. Findings revealed that both location and geometric properties are specific to landslide type and differ between them. Earthquake-induced landslides are more common near the ridge of a slope, while rainstorm-induced landslides are more frequent in the valley or near streams. The quantitative analysis of geometric properties showed that earthquake-induced landslides are generally larger and have a more compact, rounded and less complex shape. The two landslide types present different hazards, particularly in their runout zones, where dispersion of materials occurs. Insights from our quantitative approach serve as a critical foundation for informed decision-making in emergency scenarios and contribute to enhancing landslide hazard management.

KEYWORDS
earthquake, geometric properties, landslide, rainstorm, slope location

1 | INTRODUCTION

Landslides are one of the most destructive natural disasters in the world (Depicker et al., 2021; Li et al., 2009; Rana et al., 2022; Tang et al., 2010), characterized by the gravitational movement of soil, mud, rocks and debris (Cruden & Lan, 2015; Yin et al., 2014). There are various triggering factors that cause landsliding, including rainfall, earthquakes, snow melting, temperature changes, volcanic activities and human activities (Allen et al., 2015; Liu et al., 2024; Pei et al., 2023; Yang et al., 2023; Ye et al., 2022). Landslides have several typical movements such as slides, falls or flows (Hungr et al., 2014; Wang et al., 2022; Zhang et al., 2014). Among these, rainstorm- and earthquake-induced landslides are the most common ones, exhibiting distinct failure processes and characteristics (Huang et al., 2017; Huang & Montgomery, 2014; Yang & Lee, 2006; Zhang et al., 2019) and resulting in varying hazards (Meunier et al., 2008). Therefore, examining the contrasting attributes of these two landslide types is of utmost importance in understanding them and implementing effective measures to prevent landslide hazard.

The location of landslides on the slope plays a crucial role in determining landslide susceptibility, as it is directly linked to landslide connectivity (Fan et al., 2019; Meunier et al., 2008). Moreover, studies have demonstrated that the topographic site effect will affect the distribution of earthquake-induced landslides (Bouchon et al., 1996; Meunier et al., 2008). As a result, rainstorm- and earthquake-induced landslides may display distinct distribution patterns across the slope, resulting in varying levels of hazards by influencing connectivity factors (Roback et al., 2018).

Many studies have focused on assessing landslide aspect ratios, which serve to characterize geometry and facilitate their classification (Li et al., 2022; Qi et al., 2021; Sezer, 2010; Tian et al., 2017). Aspect ratios offer valuable insights into the triggering factors and formation processes of landslides (Taylor et al., 2018; Xu et al., 2014; Yang & Lee, 2006), and they are useful for landslide image interpretation

 © 2024 John Wiley & Sons Ltd.

(Keyport et al., 2018; Martha et al., 2010) and landslide risk assessment (Guzzetti, 2021; Taylor et al., 2018). Nonetheless, research on other geometric properties of landslides remains limited, with existing studies primarily examining the geometric features of a specific landslide type (Guzzetti et al., 2008; Ma et al., 2023; Milledge et al., 2014; Qu et al., 2021; Samia et al., 2017). It is important to understand that different types of movement can produce distinct shapes. For instance, in comparison with low-mobility flows, high-mobility flows often traverse longer distances, resulting in more complex shapes (Legros, 2002; Yang & Lee, 2006). For example, the high mobility and bifurcation behavior of the Sanxicun landslide in Dujiangyan, Sichuan Province, in China affected a wide area, threatening residential areas in the left valley (Gao et al., 2017). In conclusion, landslides triggered by different factors will show different geometric properties (Li et al., 2022; Rana et al., 2021) and affect different geographical areas, resulting in varying hazards and risks (Li & Lan, 2022; Liu et al., 2023; Taylor et al., 2018). However, there is a lack of comparative research on geometric properties of rainstorm- and earthquake-induced landslides. To address this gap, this study focuses on the quantitative examination of location and shape disparities of these

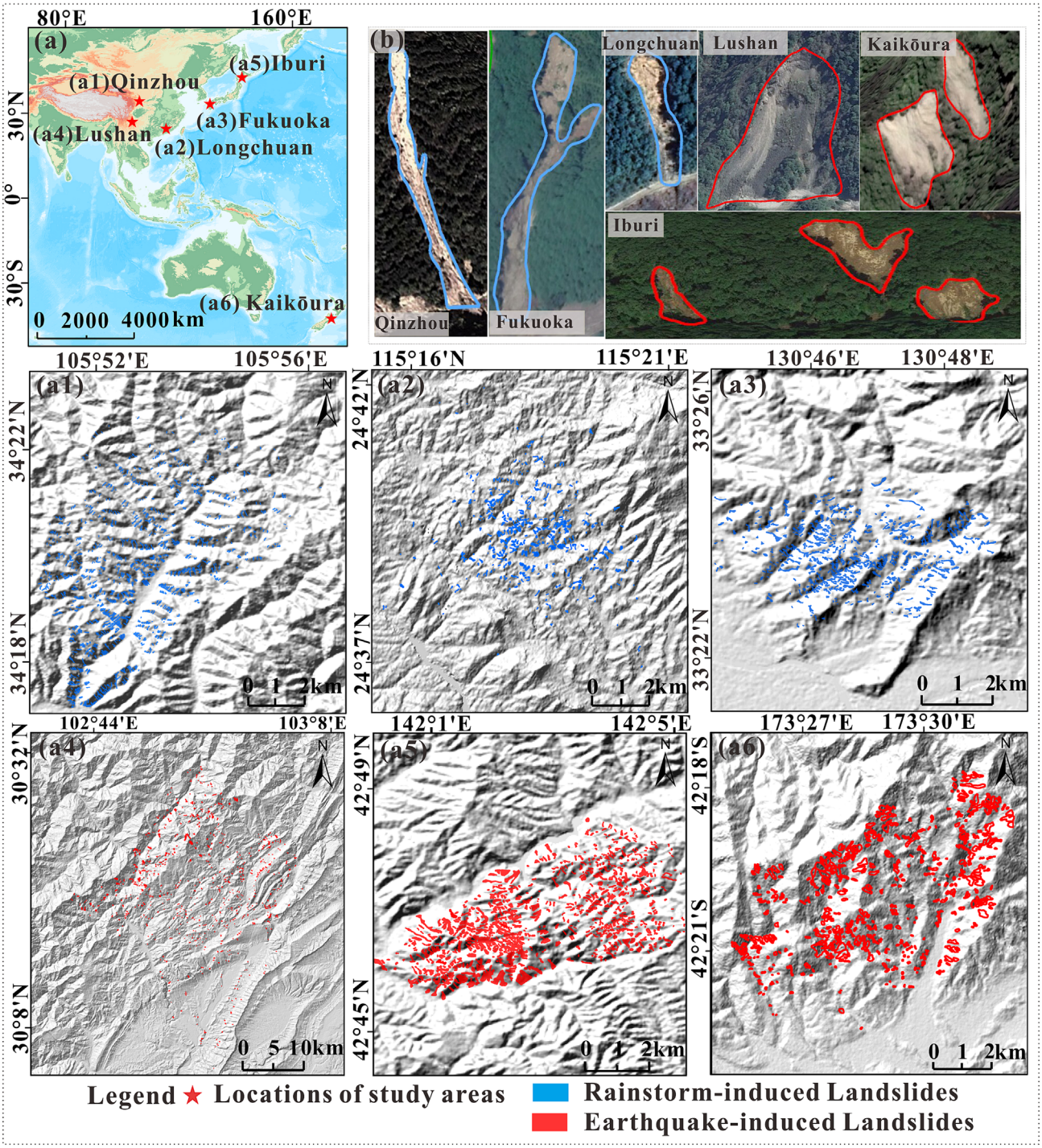


FIGURE 1 Overview of the six studied landslide areas. (a) Locations of the study areas in China, Japan, and New Zealand. (b) Images of landslide examples from all six study areas. (a1–a3) Distribution of rainstorm-induced landslides in Qinzhou, Longchuan and Fukuoka. (a4–a6) Distribution of earthquake-induced landslides in Lushan, Iburi and Kaikōura. [Color figure can be viewed at wileyonlinelibrary.com]

TABLE 1 Specific information of landslides in six study areas.

Region	State	Trigger factor	Event	Time
Qinzhou	China	Rainstorm	Four extreme rainstorm events (maximum rainfall intensity: 22 mm/h)	21 July 2013
Longchuan	China	Rainstorm	Continuous heavy rainfall (maximum rainfall intensity: 45.3 mm/h)	10–13 June 2019
Fukuoka	Japan	Rainstorm	Northern Kyushu torrential rainfall disaster (maximum rainfall intensity: 106 mm/h)	5–6 July 2017
Lushan	China	Earthquake	Lushan earthquake (M_w 6.6)	20 April 2013
Iburi	Japan	Earthquake	Hokkaido Eastern Iburi earthquake (M_w 6.6)	5 September 2018
Kaikōura	New Zealand	Earthquake	Kaikōura earthquake (M_w 7.8)	14 November 2016

two landslide types. Such an investigation holds significant implications for studying the landslide hazards and can provide new parameters for their evaluation and prediction.

We generated six landslide inventories consisting of three typical rainstorm-induced landslide areas (Qinzhou, Longchuan and Fukuoka) and three typical earthquake-induced landslide areas (Lushan, Iburi and Kaikōura). We investigated their relative locations on the slope, examined their shapes using multiple geometric properties and analysed the differences between these two types of landslides.

2 | STUDY AREAS

2.1 | Study areas of rainstorm-induced landslides

The landslides in Qinzhou occurred in a small basin in the southeast of Qinzhou District, Tianshui City, China (Figure 1a1). The region has a continental climate in the winter and a warm temperate monsoon climate in the summer, characterized by distinct seasonal rainfall patterns with a rainy season between June and September and a rainfall peak in July. Extreme rainstorm in Tianshui on 21 July 2013 (Table 1) caused extensive landsliding, mainly as shallow landslides (He et al., 2021).

Longchuan County belongs to Heyuan City in the northeast of Guangdong Province of China (Figure 1a2). Within the 4 days from 10 to 13 June 2019, cumulative heavy rainfall of 270 mm occurred, with a maximum hourly rainfall of nearly 50 mm (Table 1). While the event resulted in numerous landslides across the county, Mibei Village near Beiling Town was particularly hit hard (Feng et al., 2022).

The landslide in Fukuoka occurred in a mountainous basin in the east of Fukuoka Prefecture, Kyushu, Japan (Figure 1a3). The region falls within a warm climate zone that experiences rainfall throughout the year, with a rainy season from June to September (Miura & Nagai, 2020). On 5–6 July 2017, a rainstorm with a maximum hourly rainfall of 106 mm triggered by Typhoon No. 3 hit the northern part of Kyushu Island (Table 1) and triggered numerous landslides and massive flooding (Dou et al., 2020).

2.2 | Study areas of earthquake-induced landslides

On 20 April 2013, a 6.6 M_w earthquake with a focal depth of 13 km and an epicentre at 30.3°N and 103°E struck Lushan County, Ya'an City, in the Sichuan Province of China (Table 1). The earthquake occurred in the southwest of the Longmenshan Fault zone and caused several landslides, of which some impounded lakes (Cui et al., 2014; Xu et al., 2015). In this study, we selected landslides that were distributed across Lushan and Baoxing counties (Figure 1a4).

On 5 September 2018, a 6.6 M_w earthquake with an epicentre at 42.72°N and 142.0°E hit Iburi in the Iburi Subprefecture, located in the southern part of Hokkaido Island of Japan (Table 1). The earthquake was caused by the rupture of a blind reverse slip fault with an N–S trending strike, resulting in an average uplift of 7 cm in close proximity to the fault (Kasai & Yamada, 2019; Wang et al., 2019). The study area in eastern Iburi encompasses a portion of a small watershed in the east of the affected region (Figure 1a5), where many landslides were triggered, mainly shallow landslides (Wang et al., 2019).

On 14 November 2016, a 7.8 M_w earthquake with a focal depth of 13 km and an epicentre at 42.69°S and 173.02°E occurred in the northeast of South Island, New Zealand (Table 1). The earthquake significantly affected the coastal and inland areas in the northeast of South Island (Tanyaş et al., 2022), resulting in numerous landslides. The study area in Kaikōura encompasses a portion of a small watershed in the south of the affected region (Figure 1a6).

3 | MATERIALS AND METHODS

3.1 | Visual interpretation and landslide inventories

Landslides caused by heavy rainstorms and earthquakes are often numerous and widely distributed, which makes it challenging to conduct comprehensive field investigations (Wu et al., 2020). The availability of high-resolution remote sensing images offers the opportunity for a more detailed visual landslide analysis (Tian et al., 2016; Xu et al., 2015). In this study, we utilized the optical images from GeoEye, WorldView, SPOT-4, IKONOS and Pleiades for a visual interpretation of the landslides (Table 2). The interpretation followed the principles by Tsou et al. (2018): (1) identifying and mapping all landslides visible in the images; (2) delineating the landslide boundaries, encompassing the headscarps and bodies of all the landslides, including the source, transportation and deposition areas; (3) dividing the landslide complex into individual for accurate mapping; and (4) ensuring the interpretation accuracy by considering the image contrast before and after the event.

Based on visual interpretation, we selected representative landslide sites in all six study areas. Footprints of some landslides can be

TABLE 2 Remote sensing imagery utilized in this study.

Region	Date, before event	Sources	Resolution	Date, after event	Sources	Resolution
Qinzhou	2010/4/30	GeoEye	0.45 m	2013/10/8	GeoEye	0.43 m
				2013/12/9	Pleiades	0.5 m
Longchuan	2019/1/24	Pleiades	0.5 m	2021/1/14	Pleiades	0.5 m
Fukuoka	2017/4/22	WorldView	0.57 m	2017/9/13	WorldView	0.59 m
Lushan	2011/4/9	SPOT-4	6.25 m	2013/11/17	IKONOS	0.85 m
	2013/1/22	Pleiades	0.5 m	2015/4/15	GeoEye	0.46 m
Iburi	2017/10/24	WorldView	0.48 m	2018/9/11	WorldView	0.39 m
Kaikōura	2016/3/26	GeoEye	0.5 m	2016/11/14	WorldView	0.58 m

found in Figure 1b. New inventories were developed for Longchuan including 414 landslides, Fukuoka including 519 landslides and Lushan including 878 landslides. For the other study areas, existing inventories were modified and updated: Qinzhou including 1004 landslides based on He et al. (2021), Iburi including 792 landslides using data from the Japanese Institute of Land and Geography (available at https://github.com/koukita/2018_09_06_atumatyou) and Kaikōura including 568 landslides based on Tanyaş et al. (2022).

3.2 | Landslide location analysis

To study differences in the distribution of rainstorm- and earthquake-induced landslides, we quantified landslide locations across the slope. The location of a landslide can be described by three parameters (Meunier et al., 2008): (1) distance from the top of the landslide to the top of the slope (ridge); (2) distance between the bottom of the landslide and the nearest slope bottom (valley or stream); and (3) length of the landslide measured along the steepest longitudinal profile. We first generated the networks for ridges and valleys or streams and measured the distances described by the above three parameters using the WhiteboxTools functionality available for ArcGIS. Then we yielded relative distances between the landslides and the top and bottom of the hillslope according to the above three parameters: The normalized distance to the ridge is obtained by calculating the ratio of the distance from the top of the landslide to the top of the slope over the total length of the slope. Similarly, the normalized distance to the valley or stream is determined by the ratio of the distance from the bottom of the landslide to the bottom of the slope over the total length of the slope.

3.3 | Geometric properties analysis

Landslide shape helps in understanding the physical mechanism of landsliding processes (Milledge et al., 2014; Pourghasemi et al., 2014). The geometric properties include various metrics such as area, perimeter, major and minor axis of fitted ellipse and roundness (Rana et al., 2021). Due to the strong correlation of some properties, we only choose convex hull-based measure (C_h) (Rana et al., 2021), roundness (Samia et al., 2017) and ellipticity index (e) (Taylor et al., 2018) to quantify the compactness, circularity and complexity of landslides, respectively. In addition, the most commonly used areas are selected to measure the geometric properties of landslides.

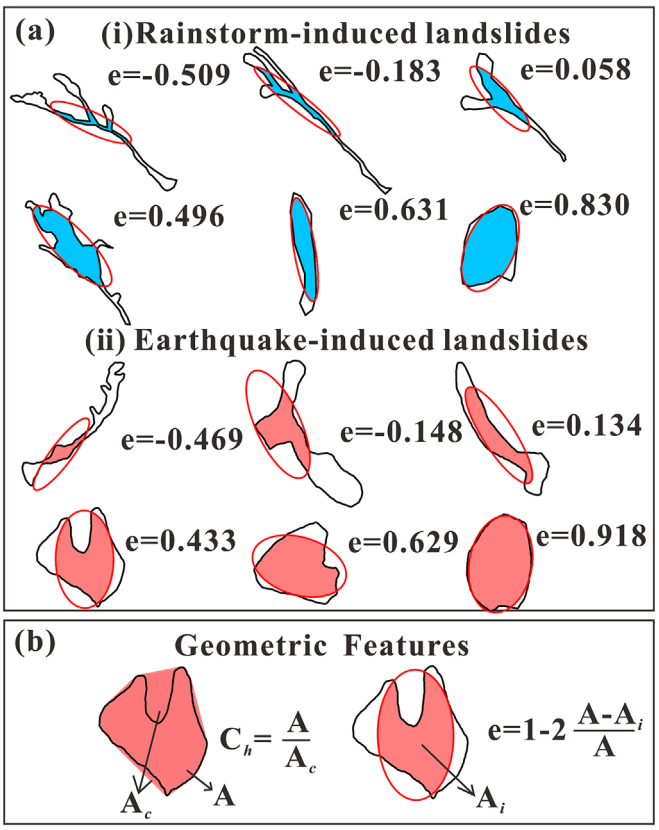


FIGURE 2 Landslide morphology mapping. (a) Fitting ellipse of rainstorm- and earthquake-induced landslides; (b) schematic diagram of geometric properties analysis, where A represents the landslide area, A_c represents the convex hull area fitted to the landslide polygon, and A_i represents the overlapping area of the original landslide and the fitted ellipse. [Color figure can be viewed at wileyonlinelibrary.com]

3.3.1 | Modeling landslide size distribution

Regardless of the triggering factors—rainfall, earthquake or human intervention—and geological settings, the existence of power-law distribution in landslide inventories is universal (Chen et al., 2017; Guo et al., 2017; Jain et al., 2022; Kasai & Yamada, 2019). For small landslides, the probability of failure will increase with increasing size but decrease after reaching a size threshold or 'rollover' (Kasai & Yamada, 2019; Malamud et al., 2004). The probability-size distribution of landslides can be obtained by calculating its probability density function (Chen et al., 2017; Malamud et al., 2004):

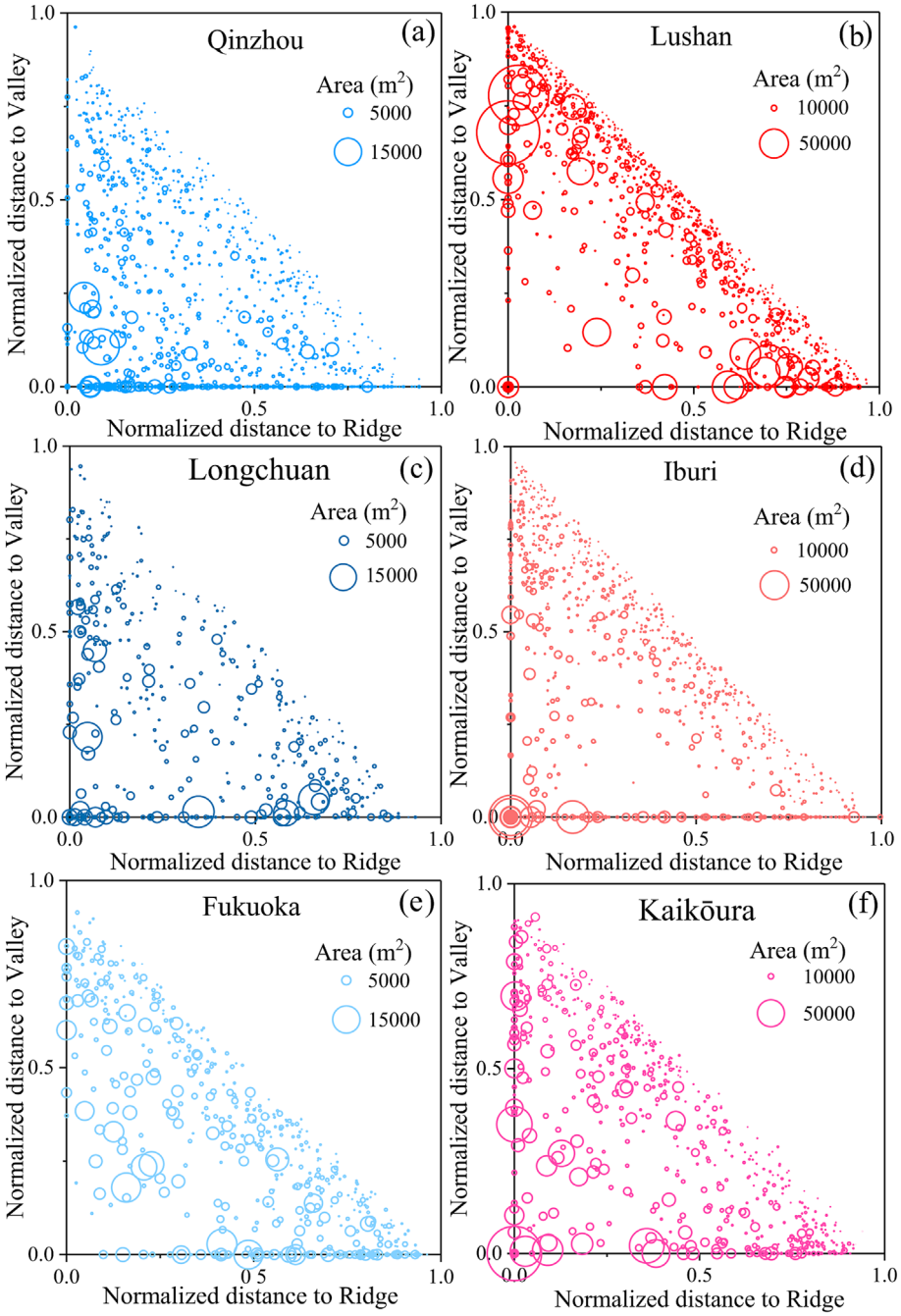


FIGURE 3 Locations of the mapped landslides in the six study areas. The x-axis represents the normalized distance from the top of a landslide to the ridge of the hillslope, while the y-axis represents the normalized distance from the bottom of a landslide to the bottom of the hillslope. The size of the circle represents landslide area. (a,c,e) rainstorm-induced landslides in Qinzhou, Longchuan and Fukuoka; (b,d,f) earthquake-induced landslides in Lushan, Iburi and Kaikōura. [Color figure can be viewed at wileyonlinelibrary.com]

$$P(A) = \frac{1}{NLT}\frac{\delta NL}{\delta A} \quad (1)$$

where $P(A)$ is the probability density function, N_{LT} is the total number of landslides, δN_L is the number of landslides with areas between A and $A + \delta A$, and δA is the increment of landslide area (m^2).

The calculated landslide probability density can be described by the three-parameter inverse gamma probability distribution proposed by Malamud et al. (2004):

$$P(A) = \frac{1}{a\Gamma(\rho)}\left[\frac{a}{A-s}\right]^{\rho+1} exp\left[-\frac{a}{A-s}\right] \quad (2)$$

where ρ controls the power-law decay of medium and large landslide sizes, a(m^2) controls the maximum probability density of landslide distribution, and s(m^2) controls the rate of decay of small landslide sizes.

3.3.2 | Analysis of compactness, circularity and complexity

C_h is the measurement based on convex hull (Figure 2b), with values from 0 to 1. A larger C_h indicates a more compact landslide shape (Rana et al., 2021). Roundness is a simple morphological measure, which is defined as the ratio of landslide area to theoretical circle area with the same perimeter of the landslide (Apaydin et al., 2006; Huang et al., 2017) with values from 0 to 1. The larger the value, the closer the shape is to a circle. To estimate the ellipticity index (e), ellipse fitting is performed according to landslide shape by using the open method (https://github.com/faithatron/Landslide_shape_tools/). This method first fits an approximate ellipse depending on landslide shape, and then scales the area of the ellipse to the approximate size of the original landslide shape. The scaling does not affect the ellipse shape, but it can produce a better area matching between the ideal ellipse

shape and the original landslide shape (Taylor et al., 2018). The ellipticity index (e) ranges between −1 and 1 (Figure 2b): If the original landslide shape does not overlap with the fitted ellipse at all ($A_i = 0$), then $e = -1$; if the original landslide shape overlaps with the fitting ellipse by 50% ($A_i = 0.5$), then $e = 0$; if the original landslide shape overlaps with the fitting ellipse by 100% ($A_i = 1$), then $e = 1$. Figure 2a shows the fitting ellipses of some of our mapped rainstorm- and earthquake-induced landslides.

4 | RESULTS

4.1 | Distribution of landslides across the slope

Figure 3 displays the distribution of landslides across the slope, where circle size represents landslide area. Circles along the x-axis indicate that landslides are distributed along the valley or near a stream, while those along the y-axis indicate that landslides are distributed along the ridge. Circles near the origin indicate that landslides stretch from the ridge to the valley or stream across the entire slope, while circles far from the two axes indicate that landslides occur in the middle section of the slope.

In Qinzhou, 64.74% of landslides are located in the lower half of the slope, that is, they tend to occur along valleys or streams, and up to 45.22% of landslides in the lower quarter of the slope, that is, they are strongly clustered near valleys or streams (Figure 3a). In Longchuan, 56.97% of landslides are in the lower half of the slope (Figure 3c). In Fukuoka, 63.58% of landslides are in the lower half of the slope, and 32.37% of landslides are in the lower quarter of the slope (Figure 3e). As for the earthquake-induced landslides, 53.59% of landslides in Lushan are located in the upper half of the slope, 31.47% of the landslides are in the upper quarter of the slope, 45.72% of

TABLE 3 Characteristics of landslide size in the six study areas, and ρ and a fitted by three-parameter inverse gamma probability density function.

Region	Qinzhou	Longchuan	Fukuoka	Lushan	Iburi	Kaikōura
Trigger factor	Rainstorms			Earthquakes		
Minimum landslides area (m^2)	91	109	161	189	187	212
Maximum landslides area (m^2)	22,384	19,625	18,165	119,717	83,907	112,450
Mean landslides area (m^2)	1366	2451	2690	5362	4181	8189
Coefficient of variation	1.219	1.1	1.001	1.819	1.517	1.291
ρ	2.034	2.179	2.058	1.625	1.804	1.825
a	1921	4499	4776	4992	5165	11072
R^2	0.993	0.994	0.994	0.997	0.997	0.996

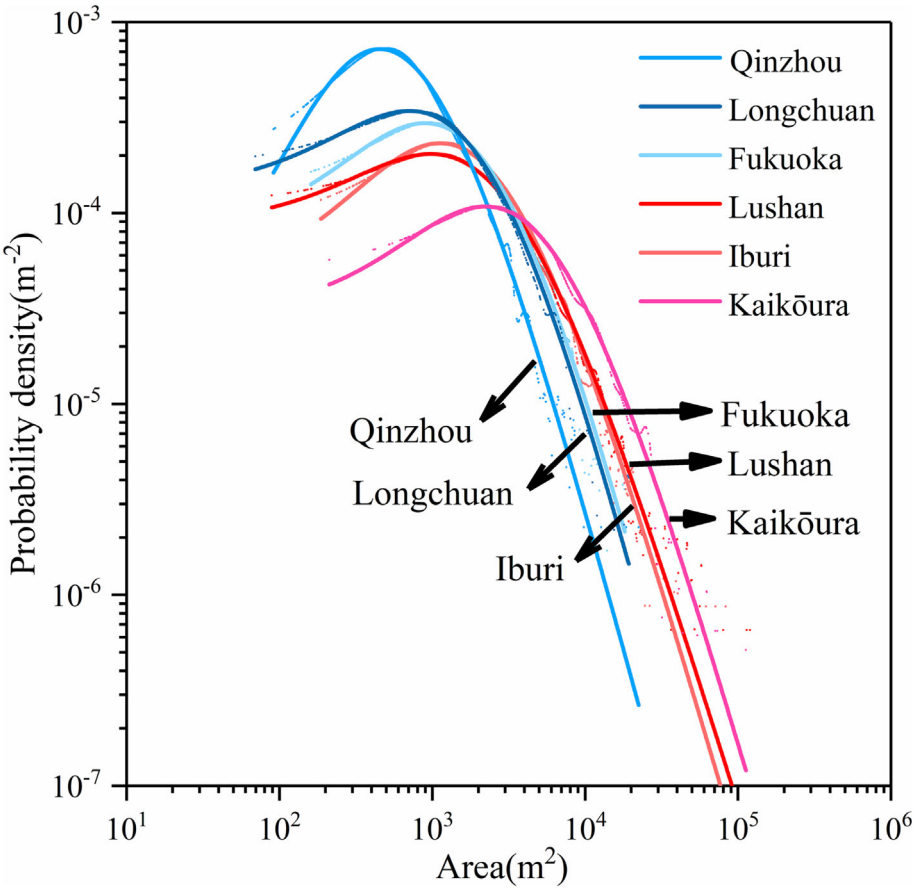


FIGURE 4 Size distribution of landslides, plotting the probability density of landslide area in logarithmic bins. They can fit the three-parameter inverse gamma probability distribution with different parameter values. Landslides in Qinzhou, Longchuan and Fukuoka were rainstorm-induced, while landslides in Lushan, Iburi and Kaikōura were earthquake-induced. [Color figure can be viewed at wileyonlinelibrary.com]

landslides are in the lower half of the slope, and 22.12% of landslides are in the lower quarter of the slope (Figure 3b). In Iburi, 54.55% of the landslides are located in the upper half of the slope, 39.9% of the landslides are in the upper quarter of the slope, 42.42% of landslides are in the lower half of the slope, and 17.42% of landslides are in the lower quarter of the slope (Figure 3d). In Kaikōura, 52.02% of the landslides are located in the upper half of the slope, 33.39% of the landslides are in the upper quarter of the slope, 47.27% of landslides are in the lower half of the slope, and 26.88% of landslides are in the lower quarter of the slope (Figure 3f). These results showed that rainstorm- and earthquake-induced landslides express distinct distribution patterns across a slope. While rainstorm-induced landslides are spatially concentrated in the lower part of slopes near valleys and streams, earthquake-induced landslides occur across the entire slope with a slight preference for its upper half near the ridge. These findings are supported by results from previous research (Chang et al., 2007; Densmore & Hovius, 2000; Huang et al., 2017; Meunier et al., 2008).

4.2 | Differences in geometric properties

4.2.1 | Difference in landslide size

Table 3 presents the landslide size characteristics within the six study areas, displaying their mean area and coefficient of variation in landslide area. Overall, the size of earthquake-induced landslides tends to be larger than that of rainstorm-induced ones. However, there is a significant variation in the size of earthquake-induced landslides, as indicated by the coefficient of variation. This variation can be attributed to the presence of some particularly large-size landslides.

The frequency-size distribution of landslides within the six study areas is shown in Figure 4. The three-parameter inverse gamma probability distribution fits well the landslide size distribution (Table 3). The probability of landslide occurrence in the small-size landslide class increases with an increase in area and rolls in some places, followed by power-law decays. The parameter ρ controls the power-law attenuation and is used to not only quantify the total erosion caused by

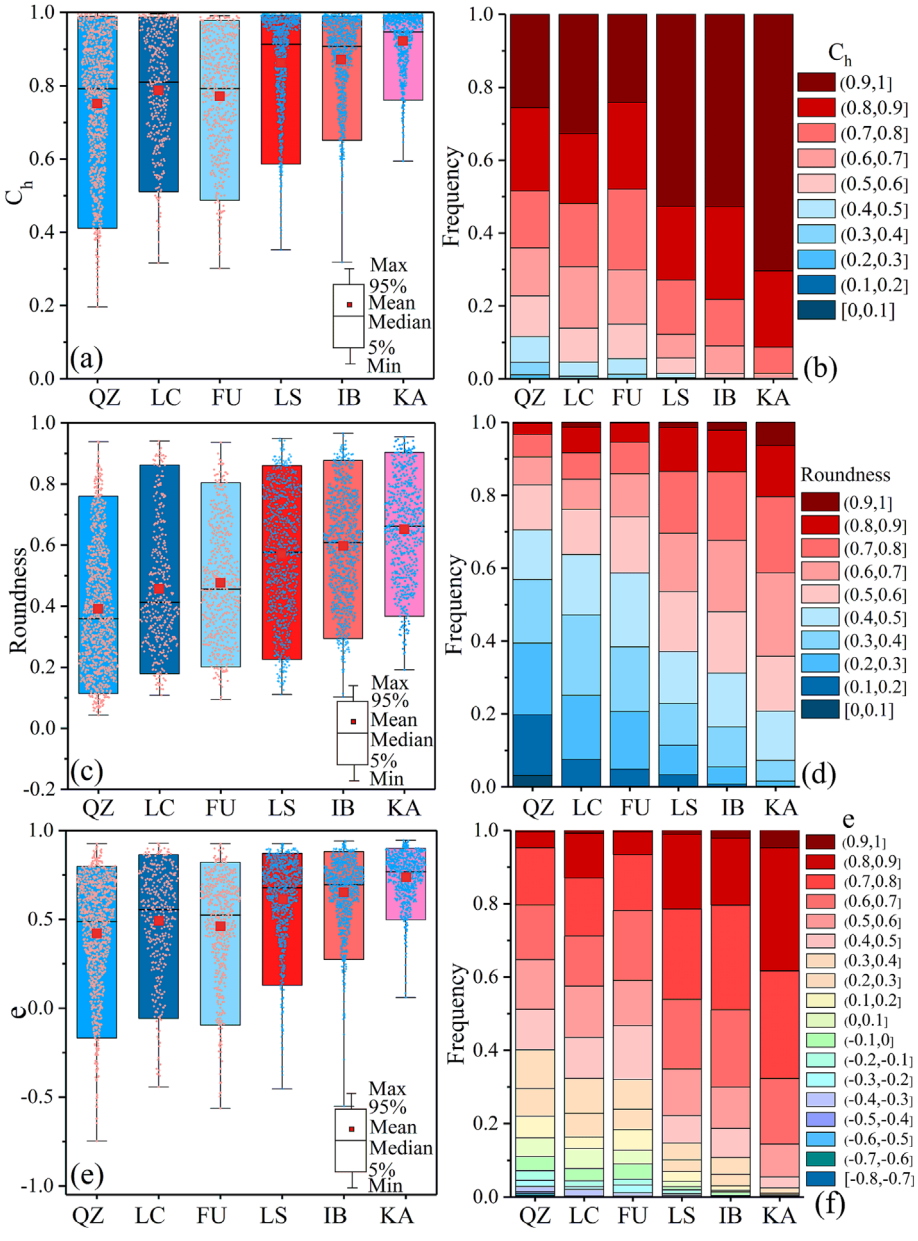


FIGURE 5 Distribution of geometric properties of landslides. (a,b) Convex hull (C_h); (c,d) roundness; and (e,f) ellipticity index (e). Landslides in Qinzhou (QZ), Longchuan (LC) and Fukuoka (FU) were rainstorm-induced, while those in Lushan (LS), Iburi (IB) and Kaikōura (KA) were earthquake-induced. [Color figure can be viewed at wileyonlinelibrary.com]

landslides but also to quantify landslide hazard (Guzzetti et al., 2005; Tanyaş et al., 2022). The larger ρ for rainstorm-induced landslides proofs their faster area decay, which is also demonstrated by the fitting curve (Table 3 and Figure 4). In addition, this difference in ρ partially reflects on the dominance of larger landslides: the lower the power-law exponent, the greater the share of larger landslides in all landslides (Borgomeo et al., 2014; Fan et al., 2019). This is true for the three earthquake-induced landslide areas in our study, where larger failures are more frequent, whereas they are not in the three rainstorm-induced landslide areas. Earthquake-induced landslides display a higher rollover position *A* (Table 3), indicating a larger median landslide size (Kasai & Yamada, 2019).

4.2.2 | Difference in convex hull, roundness and ellipticity index

We calculated the three geometric properties convex hull (C_h), roundness, and ellipticity index (e) for all landslides in the six study areas (Figure 5). We found that the mean and median values of convex hull (C_h), roundness and ellipticity index (e) are higher for the earthquake-induced landslides (Figure 5). There are numerous high convex hull values in all six landslide inventories (Figure 5a). In all three earthquake-induced landslide areas, up to 53% of landslides in Lushan and Iburi have a C_h value between 0.9 and 1, of which 70% of landslides in Kaikōura have a C_h value between 0.9 and 1. In contrast, the convex hull (C_h) is more evenly distributed between 0.7 and 1 in the rainstorm-induced landslide areas (Figure 5b). It can be concluded that earthquake-induced landslides generally have a more compact shape. Roundness for rainstorm-induced landslides varies among the three study areas: 80% of landslides in Qinzhou have values between 0.1 and 0.6, 68% of landslides in Longchuan have values between 0.2 and 0.6, and 81% of landslides in Fukuoka have values between 0.2 and 0.7 (Figure 5d). In comparison, for the most earthquake-induced landslides, roundness ranges from 0.3 to 0.9 in all three study areas (Figure 5c). This demonstrates that earthquake-induced landslides are generally more rounded in shape. Ellipticity index values range from 0.3 to 0.8 for most rainstorm-induced landslides and from 0.5 to 0.9 for most earthquake-induced landslides (Figure 5f), suggesting that rainstorm-induced landslides have a more complex shape.

Figure 6 displays the coefficient of variation for all three properties. Rainstorm-induced landslides exhibit a significant scattering for all three properties, indicating considerable morphological differences between individual landslides. This scattering might be attributed to the fluidity of rainstorm-induced landslides, where landslides of higher mobility tend to follow irregular flow trajectories or form more branches, resulting in an increased hazard potential (Legros, 2002; Taylor et al., 2018; Yang & Lee, 2006).

We also conducted significant difference tests for all three geometric properties. The nonparametric Mann–Whitney *U* test was

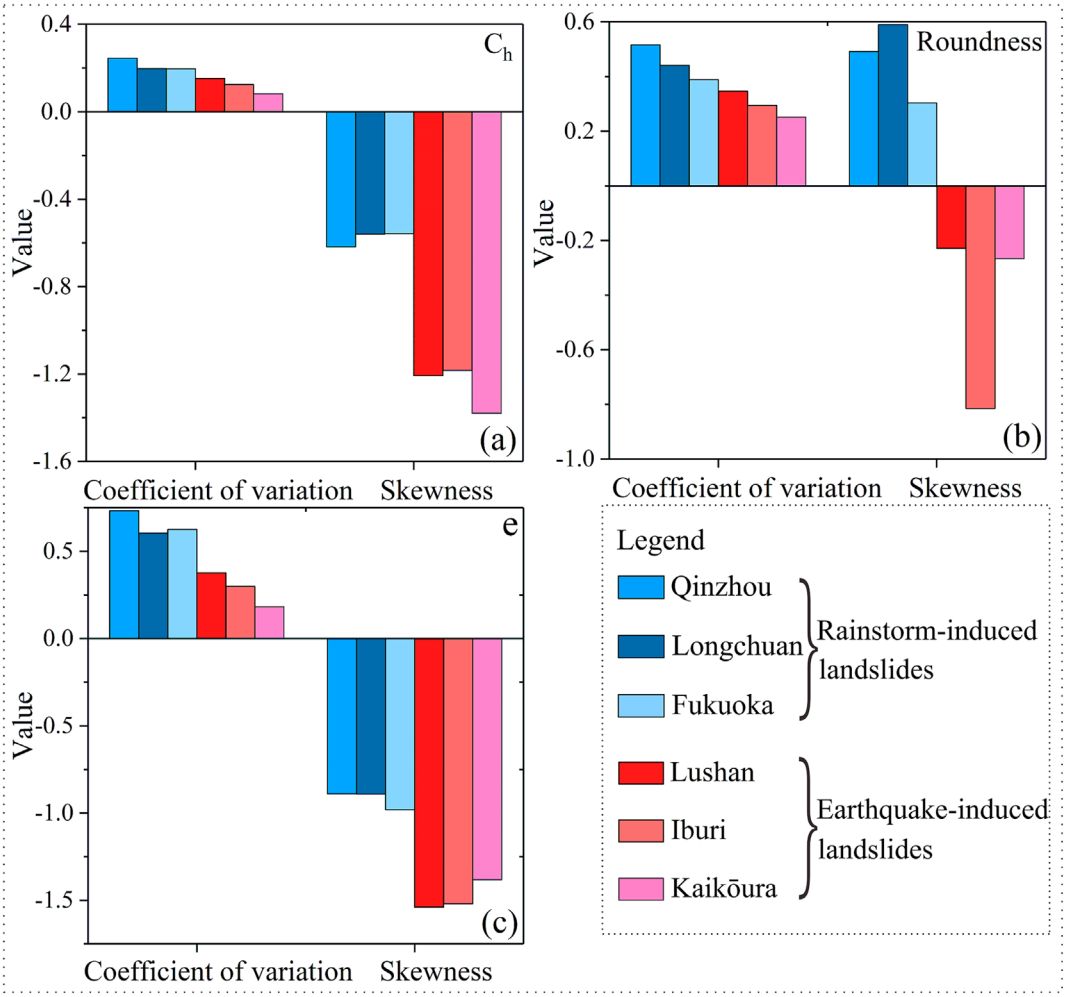


FIGURE 6 Coefficient of variation and skewness of geometric properties. (a) Convex hull (C_h), (b) roundness and (c) ellipticity index (e). [Color figure can be viewed at wileyonlinelibrary.com]

conducted for pairs of rainstorm- and earthquake-induced landslides. All pairs had a $p < 0.01$, expressing significant differences between the two landslide types. In summary, the shape of a landslide can reveal its trigger (Rana et al., 2021).

4.2.3 | Differences in probability density distribution

We analysed the probability density distribution for the three geometric properties (Rana et al., 2021) and found significant differences between the rainstorm- and earthquake-induced landslides, which provides further confirmation of our results (Figure 7).

Rainstorm-induced landslides show the highest probability density for convex hull (C_h) values of around 0.89 in Qinzhou, 0.92 in Longchuan and 0.87 in Fukuoka (Figure 7a). Earthquake-induced landslides have the highest probability density for C_h values of around 0.97 in Lushan, 0.96 in Iburi and 0.98 in Kaikōura (Figure 7a). Notably, the highest probability density of earthquake-induced landslides in Lushan and Iburi is more than twice that of rainstorm-induced landslides, and that in Kaikōura is more than four times higher (Figure 7a). At the same time, skewness is in a state of left deviation in all study areas (Figure 6a). The probability density distributions for roundness are different from those of convex hull (C_h) and ellipticity index (e), mainly regarding their skewness: Rainstorm-induced landslides show right deviation, while earthquake-induced landslides show left deviation (Figure 6b). The landslides in Qinzhou, Longchuan and Fukuoka have the highest probability density equal to 1.91, 2.14 and 1.94, respectively, in correspondence to roundness values of 0.25, 0.35 and 0.43 (Figure 7b). On the other hand, the landslides in Lushan, Iburi and Kaikōura have the highest probability density equal to 1.64, 1.98 and 2.24, respectively, in correspondence to roundness values of 0.72, 0.62 and 0.67 (Figure 7b). The probability density distributions show a left deviation for both the ellipticity index (e) and convex hull (C_h) (Figure 6c). Rainstorm-induced landslides have the highest probability density for the ellipticity index (e) near 0.65 in Qinzhou, Longchuan and Fukuoka, while earthquake-induced landslides have the highest probability density near 0.77 in Lushan, 0.73 in Iburi and 0.81 in Kaikōura. The highest probability density for the ellipticity index (e) of earthquake-induced landslides in Lushan and Iburi is about 1.5 times that of rainstorm-induced landslides, and that of earthquake-induced landslides in Kaikōura is more than twice that of rainstorm-induced landslides (Figure 7c). These results support our conclusion that, when compared with rainstorm-induced landslides, earthquake-induced landslides are more compact and rounded, but less complex.

5 | DISCUSSION

The geometric properties of a landslide are influenced by its individual trigger. Rainstorms and earthquakes are common triggers and result in landslides of particular location and shape (Huang & Montgomery, 2014; Yang & Lee, 2006). In this study, we quantified the geometric properties of rainstorm- and earthquake-induced landslides and their location on the slope in six study areas in China, Japan and New Zealand.

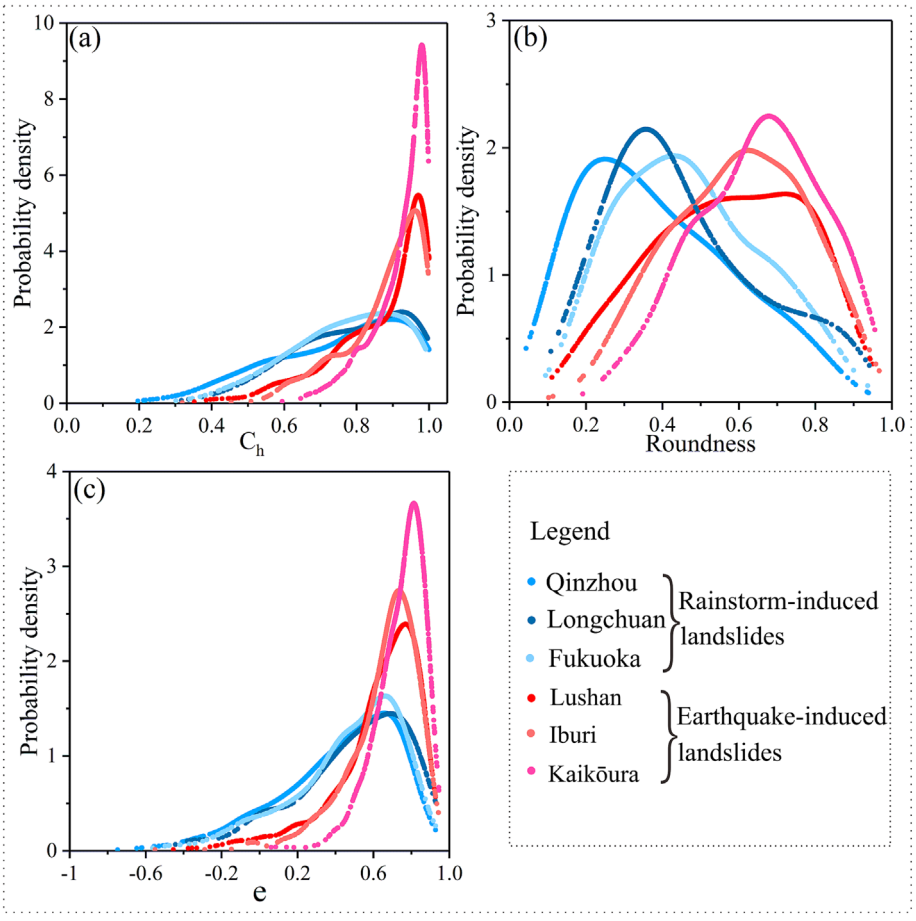


FIGURE 7 Probability density distribution of three geometric properties. (a) Convex hull (C_h), (b) roundness and (c) ellipticity index (e). [Color figure can be viewed at wileyonlinelibrary.com]

The two landslide types showed different distribution patterns regarding the normalized distance from landslides to ridges and valleys or streams. This supports Densmore & Hovius (2000), who noticed that rainstorm- and earthquake-induced landslides in Tachia basin occurred in different locations across the slope: Earthquake-induced landslides are concentrated near the ridge as a result of the topographic amplification effect, while rainstorm-induced landslides occur mainly at the bottom of the slope reflecting on the role of groundwater seepage in landsliding (Crosta & Prisco, 1999; Huang & Montgomery, 2014; Lourenço et al., 2006). Previous studies used various geometric properties of landslides as the feature space for the machine-learning classifier random forest and successfully classified different landslide types (Rana et al., 2022), but few studies have discussed differences in the geometric properties themselves. We here used area, convex hull (C_h), roundness and ellipticity index (e) of landslides to demonstrate that significant differences in geometric properties between rainstorm- and earthquake-induced landslides exist. Compared with the rainstorm-induced landslides, earthquake-induced landslides have a larger area as well as a more compact, rounded and less complex shape.

Rainstorm- and earthquake-induced landslides differ also in their related hazard (Guzzetti, 2021; Qiu et al., 2020; Ye et al., 2024). The location of a landslide on the slope is directly related to the connectivity of landslides and, hence, will affect the proportion of landslide materials transferred to the river and the underlying process (Fan et al., 2019) and affect landslide sensitivity (Meunier et al., 2008). Meunier et al. (2008) also found that there is a wide consistency between patterns of landslide position and the susceptibility in the region, and the landslide patterns has obvious dependence on the trigger mechanism. Our results show that rainstorm-induced landslides are more sensitive near valleys or streams, while earthquake-induced landslides are more sensitive near ridges. Furthermore, landslides at the base of slopes that cause destruction to houses provide a greater practical risk when there are buildings nearby the bottom of the hillslope, so we will focus our attention on the landslide caused by rainstorm near the slope's base under the circumstances. In addition, the landslide hazard map shows not only the possibility of landslide formation at a specific location but also the possibility that it might travel downslope a specified distance (Jain et al., 2022). For example, the more complex and dispersed the shape, the longer the moving distance and the larger the area of the landslide, the larger the attack range and the higher the harmfulness (Li & Lan, 2022). A landslide in Xinmo, Maoxian County, in the Sichuan Province of China not only buried the village directly in its path but also damaged some houses to the northwest because of its lateral dispersion in the runout zone (Huang et al., 2019), which explains that the complexity in shape increases landslide hazard. Therefore, it is very important to know the size and shape of landslides induced by different trigger. When we have a deeper understanding of the location and shape of a certain type of landslide, we can add additional parameters to the landslide risk assessment. However, at present, there are only some studies that quantify the scale of landslides to express the potential danger degree of landslides, and the frequency-size analysis of landslide inventory is the premise of reliable landslide hazard assessment (Jain et al., 2022; Li & Lan, 2022). The application of landslide distribution patterns and other landslide geometric characteristics in landslide risk analysis has not been quantitatively studied up to now, but only some qualitative analysis, which needs further study.

6 | CONCLUSION

This study identified differences in location and geometric properties between rainstorm-induced landslides in Qinzhou, Longchuan and Fukuoka and earthquake-induced landslides in Lushan, Iburi and Kaikōura. Rainstorm-induced landslides tend to occur near valleys or streams, while earthquake-induced landslides tend to occur near ridges, which reflects on the influence of groundwater seepage and the topographic amplification effect on landslide formation. Compared with rainstorm-induced landslides, earthquake-induced landslides are larger, more compact, more rounded and less complex. These differences impact transport dynamics and hazard levels, particularly in the runout zone, where dispersion is common. For example, the more complex and dispersed the shape of a landslide, the longer the travel distance, and the larger the landslide area, the greater the hazard. Therefore, it is very important to know the size and shape of landslides induced by different trigger factors for landslide risk assessment, and our quantitative findings offer crucial references for effective risk management and mitigation strategies.

AUTHOR CONTRIBUTIONS

Conceptualization: Haijun Qiu. *Methodology*: Lingling Su and Haijun Qiu. *Software*: Lingling Su and Bingzhe Tang. *Formal analysis*: Lingling Su and Dongdong Yang. *Investigation*: Haijun Qiu and Lingling Su. *Visualization*: Lingling Su and Haijun Qiu. *Writing—original draft preparation*: Haijun Qiu, Ulrich Kamp and Lingling Su. *Writing—review and editing*: Haijun Qiu, Bingzhe Tang, Mohib Ullah and Ulrich Kamp. *Funding acquisition*: Haijun Qiu. *Project administration*: Haijun Qiu. *Supervision*: Haijun Qiu. All of the authors have read and agreed to the published version of the manuscript.

ACKNOWLEDGEMENTS

This work was funded by the National Natural Science Foundation of China (Grant No. 42271078), Selected Science and Technology Activity Program for Overseas Scientists (Grant No. 2022-14), Key Research and Development Program of Shaanxi (Grant No. 2024SF-YBXM-669), and The Second Tibetan Plateau Scientific Expedition and Research Program (STEP) (STEP) (Grant No. 2019QZKK0902).

DATA AVAILABILITY STATEMENT

Data available on request from the authors.

ORCID

Haijun Qiu https://orcid.org/0000-0003-0263-0025

REFERENCES

Allen, S.K., Rastner, I.P., Arora, I.M., Huggel, I.C. & Stoffel, I.M. (2015) Lake outburst and debris flow disaster at Kedarnath, June 2013: hydrometeorological triggering and topographic predisposition. *Landslides*, 13(6), 1–13.

Apaydin, H.A.L.İ.T., Ozturk, F., Merdun, H.A.S.A.N. & Aziz, N.M. (2006) Determination of the drainage basin characteristics using vector GIS. *Hydrology Research*, 37(2), 129–142. Available from: https://doi.org/10.2166/nh.2006.0011

Borgomeo, E., Hebditch, K.V., Whittaker, A.C. & Lonergan, L. (2014) Characterising the spatial distribution, frequency and geomorphic controls on landslide occurrence, Molise, Italy. *Geomorphology*, 226, 148–161. Available from: https://doi.org/10.1016/j.geomorph.2014.08.004

Bouchon, M., Schultz, C.A. & Toksöz, M.N. (1996) Effect of three-dimensional topography on seismic motion. *Journal of Geophysical Research - Solid Earth*, 101(B3), 5835–5846. Available from: https://doi.org/10.1029/95JB02629

Chang, K.T., Chiang, S.H. & Hsu, M.L. (2007) Modeling typhoon- and earthquake- induced landslides in a mountainous watershed using logistic regression. *Geomorphology*, 89(3–4), 335–347. Available from: https://doi.org/10.1016/j.geomorph.2006.12.011

Chen, C.W., Oguchi, T., Hayakawa, Y.S., Saito, H. & Chen, H. (2017) Relationship between landslide size and rainfall conditions in Taiwan. *Landslides*, 14(3), 1235–1240. Available from: https://doi.org/10.1007/s10346-016-0790-7

Crosta, G. & Prisco, C.D. (1999) On slope instability induced by seepage erosion. *Canadian Geotechnical Journal*, 36(6), 1056–1073. Available from: https://doi.org/10.1139/t99-062

Cruden, D. & Lan, H.X. (2015) Using the working classification of landslides to assess the danger from a natural slope. In: *Engineering geology for society and territory-volume 2: landslide processes*. Cham, Switzerland: Springer International Publishing, pp. 3–12. Available from: https://doi.org/10.1007/978-3-319-09057-3_1

Cui, P., Zhang, J., Yang, Z., Chen, X., You, Y. & Li, Y. (2014) Activity and distribution of geohazards induced by the Lushan earthquake, April 20, 2013. *Natural Hazards*, 73(2), 711–726. Available from: https://doi.org/10.1007/s11069-014-1100-0

Densmore, A.L. & Hovius, N. (2000) Topographic fingerprints of bedrock landslides. *Geology*, 28(4), 371–374. Available from: https://doi.org/10.1130/0091-7613(2000)28<371:TFOBL>2.0.CO;2

Depicker, A., Jacobs, L., Mboga, N., Smets, B., Van Rompaey, A., Lennert, M., et al. (2021) Historical dynamics of landslide risk from population and forest-cover changes in the Kivu rift. *Nature Sustainability*, 4(11), 965–974. Available from: https://doi.org/10.1038/s41893-021-00757-9

Dou, J., Yunus, A.P., Bui, D.T., Merghadi, A., Sahana, M., Zhu, Z., et al. (2020) Improved landslide assessment using support vector machine with bagging, boosting, and stacking ensemble machine learning framework in a mountainous watershed, Japan. *Landslides*, 17(3), 641–658. Available from: https://doi.org/10.1007/s10346-019-01286-5

Fan, X., Scaringi, G., Korup, O., West, A.J., van Westen, C.J., Tanyas, H., et al. (2019) Earthquake-induced chains of geologic hazards: patterns, mechanisms, and impacts. *Reviews of Geophysics*, 57(2), 421–503. Available from: https://doi.org/10.1029/2018RG000626

Feng, W., Bai, H., Lan, B., Wu, Y., Wu, Z., Yan, L., et al. (2022) Spatial-temporal distribution and failure mechanism of group-occurring landslides in Mibei village, Longchuan county, Guangdong, China. *Landslides*, 19(8), 1957–1970. Available from: https://doi.org/10.1007/s10346-022-01904-9

Gao, Y., Yin, Y., Li, B., Feng, Z., Wang, W., Zhang, N., et al. (2017) Characteristics and numerical runout modeling of the heavy rainfall-induced catastrophic landslide–debris flow at Sanxicun, Dujiangyan, China, following the Wenchuan ms 8.0 earthquake. *Landslides*, 14(4), 1361–1374. Available from: https://doi.org/10.1007/s10346-016-0793-4

Guo, C.W., Huang, Y.D., Yao, L.K. & Alradi, H. (2017) Size and spatial distribution of landslides induced by the 2015 Gorkha earthquake in the Bhote Koshi river watershed. *Journal of Mountain Science*, 14(10), 1938–1950. Available from: https://doi.org/10.1007/s11629-016-4140-y

Guzzetti, F. (2021) On the prediction of landslides and their consequences. In: *Understanding and reducing landslide disaster risk: volume 1 Sendai landslide partnerships and Kyoto landslide commitment*, 5th edition. Cham: Springer, pp. 3–32.

Guzzetti, F., Ardizzone, F., Cardinali, M., Galli, M., Reichenbach, P. & Rossi, M. (2008) Distribution of landslides in the upper Tiber river basin, central Italy. *Geomorphology*, 96(1-2), 105–122.

Guzzetti, F., Reichenbach, P., Cardinali, M., Galli, M. & Ardizzone, F. (2005) Probabilistic landslide hazard assessment at the basin scale. *Geomorphology*, 72(1-4), 272–299. Available from: https://doi.org/10.1016/j.geomorph.2005.06.002

He, J., Qiu, H., Qu, F., Hu, S., Yang, D., Shen, Y., et al. (2021) Prediction of spatiotemporal stability and rainfall threshold of shallow landslides using the TRIGRS and Scoops3D models. *Catena*, 197, 104999. Available from: https://doi.org/10.1016/j.catena.2020.104999

Huang, A.Y.L. & Montgomery, D.R. (2014) Topographic locations and size of earthquake- and typhoon- generated landslides, Tachia River, Taiwan. *Earth Surface Processes and Landforms*, 39(3), 414–418. Available from: https://doi.org/10.1002/esp.3510

Huang, D., Li, Y., Song, Y., Xu, Q. & Pei, X. (2019) Insights into the catastrophic Xinmo rock avalanche in Maoxian county, China: combined effects of historical earthquakes and landslide amplification. *Engineering Geology*, 258, 105158. Available from: https://doi.org/10.1016/j.enggeo.2019.105158

Huang, J.C., Milliman, J.D., Lee, T.Y., Chen, Y.C., Lee, J.F., Liu, C.C., et al. (2017) Terrain attributes of earthquake- and rainstorm- induced landslides in orogenic mountain belt, Taiwan. *Earth Surface Processes and Landforms*, 42(10), 1549–1559. Available from: https://doi.org/10.1002/esp.4112

Hungr, O., Leroueil, S. & Picarelli, L. (2014) The Varnes classification of landslide types, an update. *Landslides*, 11(2), 167–194. Available from: https://doi.org/10.1007/s10346-013-0436-y

Jain, S., Khosa, R. & Gosain, A.K. (2022) Impact of landslide size and settings on landslide scaling relationship: a study from the Himalayan regions of India. *Landslides*, 19(2), 1–13. Available from: https://doi.org/10.1007/s10346-021-01794-3

Kasai, M. & Yamada, T. (2019) Topographic effects on frequency-size distribution of landslides triggered by the Hokkaido eastern Iburi earthquake in 2018. *Earth, Planets and Space*, 71(1), 89. Available from: https://doi.org/10.1186/s40623-019-1069-8

Keyport, R.N., Oommen, T., Martha, T.R., Sajinkumar, K.S. & Gierke, J.S. (2018) A comparative analysis of pixel- and object- based detection of landslides from very high-resolution images. *International Journal of Applied Earth Observation and Geoinformation*, 64, 1–11. Available from: https://doi.org/10.1016/j.jag.2017.08.015

Legros, F. (2002) The mobility of long-runout landslides. *Engineering Geology*, 63(3–4), 301–331. Available from: https://doi.org/10.1016/S0013-7952(01)00090-4

Li, C., Tang, H., Hu, X. & Hu, L.B. (2009) Landslide prediction based on wavelet analysis and cusp catastrophe. *Journal of Earth Science*, 20(6), 971–977. Available from: https://doi.org/10.1007/s12583-009-0082-4

Li, L. & Lan, H. (2022) Complexities of landslide moving path: a review and perspective. *Earth Science*, 47(12), 4663–4680.

Li, L., Lan, H., Strom, A. & Macciotta, R. (2022) Landslide longitudinal shape: a new concept for complementing landslide aspect ratio. *Landslides*, 19(5), 1143–1163. Available from: https://doi.org/10.1007/s10346-021-01828-w

Liu, X., Su, P., Li, Y., Xia, Z., Ma, S., Xu, R., et al. (2023) Spatial distribution of landslide shape induced by Luding Ms 6.8 earthquake, Sichuan, China: case study of the Moxi town. *Landslides*, 20, 1667–1678.

Liu, Y., Qiu, H., Ulrich, K., Wang, N., Wang, J., Huang, C., et al. (2024) Higher temperature sensitivity of retrogressive thaw slump activity in the Arctic compared to the third pole. *Science of the Total Environment*, 914, 170007. Available from: https://doi.org/10.1016/j.scitotenv.2024.170007

Lourenço, S.D., Sassa, K. & Fukuoka, H. (2006) Failure process and hydrologic response of a two layer physical model: implications for rainfall-induced landslides. *Geomorphology*, 73(1–2), 115–130. Available from: https://doi.org/10.1016/j.geomorph.2005.06.004

Ma, S., Qiu, H., Zhu, Y., Yang, D., Tang, B., Wang, D., et al. (2023) Topographic changes, surface deformation and movement process before, during and after a rotational landslide. *Remote Sensing*, 15(3), 662. Available from: https://doi.org/10.3390/rs15030662

Malamud, B.D., Turcotte, D.L., Guzzetti, F. & Reichenbach, P. (2004) Landslide inventories and their statistical properties. *Earth Surface Processes*, 29(6), 687–711. Available from: https://doi.org/10.1002/esp.1064

Martha, T.R., Kerle, N., Jetten, V., van Westen, C.J. & Kumar, K.V. (2010) Characterising spectral, spatial and morphometric properties of landslides for semi-automatic detection using object-oriented methods. *Geomorphology*, 116(1–2), 24–36. Available from: https://doi.org/10.1016/j.geomorph.2009.10.004

Meunier, P., Hovius, N. & Haines, J.A. (2008) Topographic site effects and the location of earthquake induced landslides. *Earth and Planetary Science Letters*, 275(3–4), 221–232. Available from: https://doi.org/10.1016/j.epsl.2008.07.020

Milledge, D.G., Bellugi, D., McKean, J.A., Densmore, A.L. & Dietrich, W.E. (2014) A multidimensional stability model for predicting shallow landslide size and shape across landscapes. *Journal of Geophysical Research - Earth Surface*, 119(11), 2481–2504. Available from: https://doi.org/10.1002/2014JF003135

Miura, T. & Nagai, S. (2020) Landslide detection with himawari-8 geostationary satellite data: a case study of a torrential rain event in Kyushu, Japan. *Remote Sensing*, 12(11), 1734. Available from: https://doi.org/10.3390/rs12111734

Pei, Y., Qiu, H., Zhu, Y., Wang, J., Yang, D., Tang, B., et al. (2023) Elevation dependence of landslide activity induced by climate change in the eastern Pamirs. *Landslides*, 20(6), 1–19. Available from: https://doi.org/10.1007/s10346-023-02030-w

Pourghasemi, H.R., Moradi, H.R., Fatemi Aghda, S.M., Sezer, E.A., Goli Jirandeh, A. & Pradhan, B. (2014) Assessment of fractal dimension and geometrical characteristics of the landslides identified in north of Tehran, Iran. *Environmental Earth Sciences*, 71(8), 3617–3626. Available from: https://doi.org/10.1007/s12665-013-2753-9

Qi, T., Meng, X., Feng, Q., Zhao, Y. & Dijkstra, T. (2021) Distribution and characteristics of large landslides in a fault zone: a case study of the ne Qinghai-Tibet plateau. *Geomorphology*, 379, 107592. Available from: https://doi.org/10.1016/j.geomorph.2021.107592

Qiu, H., Hu, S., Yang, D., He, Y. & Kamp, U. (2020) Comparing landslide size probability distribution at the landscape scale (loess plateau and the Qinba mountains, central China) using double Pareto and inverse gamma. *Bulletin of Engineering Geology and the Environment*, 80(2), 1035–1046. Available from: https://doi.org/10.1007/s10064-020-02037-w

Qu, F., Qiu, H., Sun, H. & Tang, M. (2021) Post-failure landslide change detection and analysis using optical satellite Sentinel-2 images. *Landslides*, 18(1), 447–455. Available from: https://doi.org/10.1007/s10346-020-01498-0

Rana, K., Malik, N. & Ozturk, U. (2022) Landsifier v1. 0: a python library to estimate likely triggers of mapped landslides. *Natural Hazards and Earth System Sciences*, 22(11), 3751–3764. Available from: https://doi.org/10.5194/nhess-22-3751-2022

Rana, K., Ozturk, U. & Malik, N. (2021) Landslide geometry reveals its trigger. *Geophysical Research Letters*, 48(4), e2020GL090848. Available from: https://doi.org/10.1029/2020GL090848

Roback, K., Clark, M.K., West, A.J., Zekkos, D., Li, G., Gallen, S.F., et al. (2018) The size, distribution, and mobility of landslides caused by the 2015 mw7.8 Gorkha earthquake, Nepal. *Geomorphology*, 301, 121–138. Available from: https://doi.org/10.1016/j.geomorph.2017.01.030

Samia, J., Temme, A., Bregt, A., Wallinga, J., Guzzetti, F., Ardizzone, F., et al. (2017) Do landslides follow landslides? Insights in path dependency from a multi-temporal landslide inventory. *Landslides*, 14(2), 547–558. Available from: https://doi.org/10.1007/s10346-016-0739-x

Sezer, E. (2010) A computer program for fractal dimension (FRACEK) with application on type of mass movement characterization. *Computers & Geosciences*, 36(3), 391–396. Available from: https://doi.org/10.1016/j.cageo.2009.04.006

Tang, H., Jia, H., Hu, X., Li, D. & Xiong, C. (2010) Characteristics of landslides induced by the great Wenchuan earthquake. *Journal of Earth Science*, 21(1), 104–113. Available from: https://doi.org/10.1007/s12583-010-0008-1

Tanyaş, H., Görüm, T., Fadel, I., Yıldırım, C. & Lombardo, L. (2022) An open dataset for landslides triggered by the 2016 Mw 7.8 Kaikōura earthquake, New Zealand. *Landslides*, 19(6), 1405–1420. Available from: https://doi.org/10.1007/s10346-022-01869-9

Taylor, F.E., Malamud, B.D., Witt, A. & Guzzetti, F. (2018) Landslide shape, ellipticity and length-to-width ratios. *Earth Surface Processes and Landforms*, 43(15), 3164–3189. Available from: https://doi.org/10.1002/esp.4479

Tian, Y., Xu, C., Chen, J., Zhou, Q. & Shen, L. (2017) Geometrical characteristics of earthquake-induced landslides and correlations with control factors: a case study of the 2013 Minxian, Gansu, China, mw 5.9 event. *Landslides*, 14(6), 1915–1927. Available from: https://doi.org/10.1007/s10346-017-0835-6

Tian, Y., Xu, C., Xu, X. & Chen, J. (2016) Detailed inventory mapping and spatial analyses to landslides induced by the 2013 ms 6.6 Minxian earthquake of China. *Journal of Earth Science*, 27(6), 11.

Tsou, C.Y., Chigira, M., Higaki, D., Sato, G., Yagi, H., Sato, H.P., et al. (2018) Topographic and geologic controls on landslides induced by the 2015 Gorkha earthquake and its aftershocks: an example from the Trishuli valley, central Nepal. *Landslides*, 15(5), 953–965. Available from: https://doi.org/10.1007/s10346-017-0913-9

Wang, F., Fan, X., Yunus, A.P., Subramanian, S.S., Alonso-Rodriguez, A., Dai, L., et al. (2019) Coseismic landslides triggered by the 2018 Hokkaido, Japan (mw 6.6), earthquake: spatial distribution, controlling factors, and possible failure mechanism. *Landslides*, 16(8), 1551–1566. Available from: https://doi.org/10.1007/s10346-019-01187-7

Wang, L., Qiu, H., Zhou, W., Zhu, Y., Liu, Z., Ma, S., et al. (2022) The post-failure spatiotemporal deformation of certain translational landslides may follow the pre-failure pattern. *Remote Sensing*, 14(10), 2333. Available from: https://doi.org/10.3390/rs14102333

Wu, W., Xu, C., Wang, X., Tian, Y. & Deng, F. (2020) Landslides triggered by the 3 August 2014 Ludian (China) mw 6.2 earthquake: an updated inventory and analysis of their spatial distribution. *Journal of Earth Science*, 31(4), 853–866. Available from: https://doi.org/10.1007/s12583-020-1297-7

Xu, C., Shyu, J.B.H. & Xu, X. (2014) Landslides triggered by the 12 January 2010 Port-au-Prince, Haiti, M W= 7.0 earthquake: visual interpretation, inventory compiling, and spatial distribution statistical analysis. *Natural Hazards and Earth System Sciences*, 14(7), 1789–1818. Available from: https://doi.org/10.5194/nhess-14-1789-2014

Xu, C., Xu, X. & Shyu, J.B.H. (2015) Database and spatial distribution of landslides triggered by the Lushan, China Mw 6.6 earthquake of 20 April 2013. *Geomorphology*, 248, 77–92. Available from: https://doi.org/10.1016/j.geomorph.2015.07.002

Yang, D., Qiu, H., Ye, B., Liu, Y., Zhang, J. & Zhu, Y. (2023) Distribution and recurrence of warming-induced retrogressive thaw slumps on the Central Qinghai-Tibet plateau. *Journal of Geophysical Research - Earth Surface*, 128(8), 1–17. Available from: https://doi.org/10.1029/2022JF007047

Yang, Z.Y. & Lee, Y.H. (2006) The fractal characteristics of landslides induced by earthquakes and rainfall in central Taiwan. In10th IAEG International Congress, Nottingham, paper (no. 48).

Ye, B., Qiu, H., Tang, B., Liu, Y., Liu, Z., Jiang, X., et al. (2024) Creep deformation monitoring of landslides in a reservoir area. *Journal of Hydrology*, 2024(632), 130905. Available from: https://doi.org/10.1016/j.jhydrol.2024.130905

Ye, X., Zhu, H., Wang, J., Zhang, Q., Shi, B., Schenato, L., et al. (2022) Subsurface multi-physical monitoring of a reservoir landslide with the fiber-optic nerve system. *Geophysical Research Letters*, 49(11), e2022GL098211. Available from: https://doi.org/10.1029/2022GL098211

Yin, Z., Zhao, W. & Qin, X. (2014) Distribution characteristics of geohazards induced by the Lushan earthquake and their comparisons with the Wenchuan earthquake. *Journal of Earth Science*, 25(5), 912–923. Available from: https://doi.org/10.1007/s12583-014-0471-1

Zhang, J., van Westen, C.J., Tanyas, H., Mavrouli, O., Ge, Y., Bajrachary, S., et al. (2019) How size and trigger matter: analyzing rainfall-and

earthquake-triggered landslide inventories and their causal relation in the Koshi River basin, central Himalaya. *Natural Hazards and Earth System Sciences*, 19(8), 1789–1805. Available from: https://doi.org/10.5194/nhess-19-1789-2019

Zhang, S., Zhang, L.M. & Glade, T. (2014) Characteristics of earthquake- and rain- induced landslides near the epicenter of Wenchuan earthquake. *Engineering Geology*, 175(11), 58–73. Available from: https://doi.org/10.1016/j.enggeo.2014.03.012

How to cite this article: Qiu, H., Su, L., Tang, B., Yang, D., Ullah, M., Zhu, Y. et al. (2024) The effect of location and geometric properties of landslides caused by rainstorms and earthquakes. *Earth Surface Processes and Landforms*, 49(7), 2067–2079. Available from: https://doi.org/10.1002/esp.5816